FISEVIER

Contents lists available at ScienceDirect

# Journal of Magnetism and Magnetic Materials

journal homepage: www.elsevier.com/locate/jmmm



#### Research articles

# Oxidation of wüstite rich iron oxide nanoparticles via post-synthesis annealing

Zichun Yan <sup>a</sup>, Sara FitzGerald <sup>b</sup>, Thomas M. Crawford <sup>b</sup>, O. Thompson Mefford <sup>a,\*</sup>

- <sup>a</sup> Department of Materials Science & Engineering, Clemson University, Clemson, SC 29634, USA
- b Department of Physics and Astronomy, SmartState Center for Experimental Nanoscale Physics, University of South Carolina, Columbia, SC 29208, USA

#### ARTICLE INFO

Keywords:
Magnetic nanoparticle
Nanoparticle synthesis
Materials characterization
Oxidation
Wüstite
Magnetite

#### ABSTRACT

When forming magnetic nanoparticles, the decomposition of organo-metallic precursors causes a reduction of Fe (III) to Fe(II) which leads to the formation of an antiferromagnetic rock salt phase of FeO. The antiferromagnetic phase reduces the nanoparticle magnetization, so a new method of oxidation was developed that can convert FeO rich particles to  $Fe_3O_4$  particles. Iron oxide nanoparticles with different sizes were synthesized to validate the oxidation method. We demonstrate that iron oxide nanoparticles can be oxidized by post synthesis annealing without addition of oxidizing agents. The oxidized particles were measured with XRD, VSM and AC calorimetry to show the effective oxidation by comparing to the as prepared sample. The resulting 20 nm oxidized particles have a saturation magnetization of 72  $Fam^2/kg$  at 300 K and a specific absorption rate of 181 W/g under a 212 kHz, 33 mT AC field.

#### 1. Introduction

In recent years, developments in thermal decomposition synthesis have improved control over the size, morphology, and composition of iron oxide-based magnetic nanoparticles [1-4]. Usually the reaction requires organo-metallic complexes as precursors. As the complexes decompose at high temperature, the organic ligands also decompose and generate reducing agents such as carbon or carbon monoxide. These cause reduction of metal (typically iron, from trivalent to divalent) during the high-temperature reaction and result in the formation of unwanted wüstite structure, [5–9] which leads to a loss of magnetization this affects applications such as magnetic resonance imaging [10], magnetic hyperthermia, [11,12], and magnetic particle imaging [13,14]. To solve this problem, different approaches were developed to oxidize the divalent iron to trivalent iron inside the particles either during particle formation or after particles are synthesized. These include adding oxygen during synthesis [5,15], adding oxygen to oxidize the particles after synthesis [16], aging the particles [9,17], as well as adding solid oxidizing agents [13,18]. Although these methods succeeded in oxidizing the particles from wüstite to magnetite or maghemite to some extent, they are not perfect. For example, adding oxygen to a high-temperature organic liquid increases the risk of ignition of reagents. Adding oxidizing agents to the reaction at high

temperatures increases the possibility of oxidizing the organic ligands and requires an additional process to remove the excess.

Based on the phase diagram of iron oxide (Fig. 1), wüstite (FeO), is not a thermodynamically favorable phase at a relatively low temperature [19]. Thus the existence of wüstite in the nanoparticles was caused by quenching. As shown in Fig. 1, to transform FeO (wüstite) to Fe<sub>3</sub>O<sub>4</sub> (magnetite), one can either decrease the temperature at a certain oxygen level or increase the oxygen partial pressure at a specific temperature. In practice, this can be done easily when dealing with ceramics by sintering the iron oxide solids in a controlled stoichiometry and atmosphere. However, in the case of nanoparticles, the sintering method does not apply since it will destroy the organic ligands and cause particle merging. Theoretically, the FeO phase has a thermodynamic potential to relax to  $Fe_3O_4$  and finally  $\alpha$ - $Fe_2O_3$  (hematite) according to the phase diagram, therefore, if given enough energy to overcome the kinetic energy barrier, the phase transition process should be spontaneous. It has been previously proposed [20], that the transformation between wüstite and magnetite requires a re-coordination of iron cations which is likely to happen as both wüstite and magnetite exhibit cubic close packing. While the transformation between wüstite and hematite requires a shift of the oxygen planes from a cubic close packed arrangement to a hexagonal close packed arrangement, this process is predominantly facilitated by the anionic diffusion of oxygen. Thus, if the particles are annealed at an

E-mail address: mefford@clemson.edu (O.T. Mefford).



<sup>\*</sup> Corresponding author.

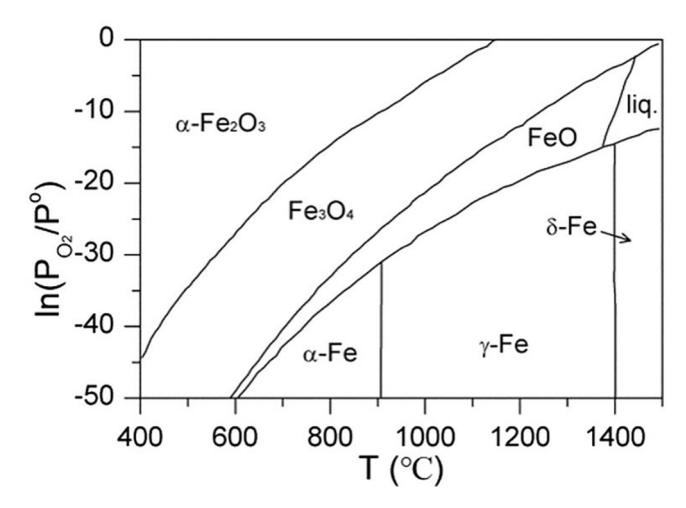


**Fig. 1.** Phase diagram of Fe-O compounds at  $400-1500~^{\circ}$ C and certain oxygen partial pressures. Figure is reprinted from ref.19 with permission. Copyright 2019 Elsevier.

ideal temperature for a sufficient time, the wüstite-rich particles will automatically turn into magnetite with minimum addition of oxygen.

Herein, we propose a facile and efficient way to convert the asprepared wüstite-rich particles into pure magnetite particles by accelerating the oxidation with annealing. The success of this conversion was confirmed via x-ray powder diffraction (XRD) and zero-field cooling/field cooling (ZFC/FC) magnetometry.

#### 2. Experimental

## 2.1. Particle synthesis and post-synthesis annealing

Thermal decomposition of oleate precursors was conducted in a "one pot" reaction that was adopted from a previous study with changes [2]. Iron (III) oleate precursors were made by reacting ferric chloride with sodium oleate in a refluxing solvent mixture of hexane, ethanol, and water prior to the particle synthesis. The iron oleate was obtained by evaporating hexane from the upper layer and precipitated by washing with acetone. The final waxy solid was dried in a vacuum oven at 80°C overnight before use. To synthesize spherical wüstite-rich nanoparticles with different diameters different quantities of reagents, reaction time, and reaction temperatures were used. Briefly, 15 nm iron oxide particles were made by refluxing 4 mmol iron (III) oleate, 4.2 mL oleic acid, and 12 mL n-octadecene at 325 °C for 1.5 h under nitrogen. 20 nm iron oxide nanoparticles were made by refluxing 9 mmol iron (III) oleate, 5 g docosane, 9 mL oleic acid, and 5 mL n-octadecene at 365 °C for 2 h under nitrogen. 30 nm iron oxide nanoparticles were made by refluxing 7.47 mmol iron (III) oleate, 3.73 mmol iron (II) oleate, 11.2 mL oleic acid, 5 g docosane, and 10 mL n-octadecene at 365°C for 2 h under nitrogen. To ensure the formation of wüstite, all reactions underwent a degassing step where the reagents were heated to 100 °C under vacuum for 1 h

To purify the products, the final product was added to a washing solution containing hexanes (5 mL), ethanol (30 mL), and acetone (30 mL); this mixture was vortexed and centrifuged at 10000 rpm for 5 min. The precipitation was collected by decanting the supernatant and repeat the washing process with the same washing solution until the supernatant became clear. The final precipitation was then redispersed and stored in hexanes.

The particles were weighed after being transferred into tared glass vials where the hexane was evaporated and were then dispersed into noctyl ether with a concentration of 20 mg/mL. To study the effect of the oxidant, the 15 nm particles were annealed at 280  $^{\circ}$ C for 1 h with or without trimethylamine N-oxide (TMAO) (0.05 mmol/mL). 30 nm

particles were annealed at 250  $^{\circ}$ C, 265  $^{\circ}$ C, and 280  $^{\circ}$ C for 1 h and 1.5 h, respectively, to study the effect of parameters during annealing. The 20 nm particles were annealed at 250  $^{\circ}$ C for 2 h to validate the annealing procedure, and the annealed particles were used for further magnetic characterizations. The resulting products were purified and stored with the same procedures mentioned above.

#### 2.2. Materials characterization

Electron microscopy, X-ray diffraction, vibrating sample magnetometry, and inductively coupled plasma-optical emission spectroscopy methods were described in Chapter 2.

#### 3. Results and discussion

#### 3.1. Particle synthesis and post-synthesis annealing

Iron oxide nanoparticles were synthesized using a relatively mature method that uses iron (III) as the thermal decomposition precursor. This method was introduced by Park et al. [2,8] and was widely used for preparing iron oxide nanoparticles with narrow size distributions. As shown in Fig. 2, spherical iron oxide particles were prepared. The size distributions for each batch were relatively narrow and the mean sizes were close to the targeted value. Higher concentration of precursors, higher reaction temperature, and longer reaction time was used to produce particles with larger sizes; however, such changes may also result in wider size distribution. The synthesized particles have mean diameters of 15.4  $\pm$  1.3 nm (targeted 15 nm), 18.6  $\pm$  1.2 nm (targeted 20 nm), and 38  $\pm$  7 nm (targeted 30 nm) respectively. It is important to mention that in Fig. 2 a) and b), some particles show what appears to be a "core/shell" like structure. This structure likely occurs because the particles are slightly oxidized on the surface before an annealing treatment. The oxidized regions are more prominent on particles with smaller sizes, like the 15 nm and 20 nm particles, while larger particles (i.e., 30 nm) do not show significant core/shell structures due to a relatively lower specific surface area [21]. This hypothesis was further confirmed by XRD analysis. Before annealing, larger particles have a higher fraction of wüstite than smaller particles. A more detailed discussion of this phase behavior can be found in the following paragraphs. The size distribution of particles after annealing remained unchanged and the core/shell images disappeared.

The 15 nm particles were used for the study of oxidation via the addition of oxidizing agents. Before oxidation the as-prepared 15 nm iron oxide nanoparticles showed a combination of spinel and rock salt phase as illustrated in Fig. 3. According to the Rietveld refinement, the weight fraction of the spinel phase is approximately 83% and the weight fraction of the rock salt phase is around 17%. Such particles were treated by the annealing methods with or without the addition of oxidizing agents. As described in previous studies, TMAO or oxygen were typically used as an oxidizing agent for the post-synthesis oxidation of iron oxide nanoparticles. Herein, we hypothesized that the addition of oxidizing agents was not the critical factor that converted wüstite to magnetite; if given enough thermal energy and annealing time, particles could be converted to pure spinel without adding any oxidizing agents. A set of control experiments were conducted with the as-prepared 15 nm iron oxide nanoparticles by controlling the parameters during annealing. As shown in Fig. 3, the four groups with post-synthesis treatment had very similar XRD results, and they all exhibit a pure spinel structure. This indicates that the driving force of converting rock salt phase to spinel phase is not the addition of oxidizing agents since even the sample with no addition of TMAO or air (orange line, Wüstite-anneal-N2) showed a 100% spinel structure. Most likely, the anneal process was done without a degassing procedure and the oxygen that dissolved in the organic solvent (n-octyl ether) is enough for the oxidation of wüstite to magnetite [22,23]. It is important to check the reproducibility of the annealing process. To further validate the hypothesis, wüstite particles

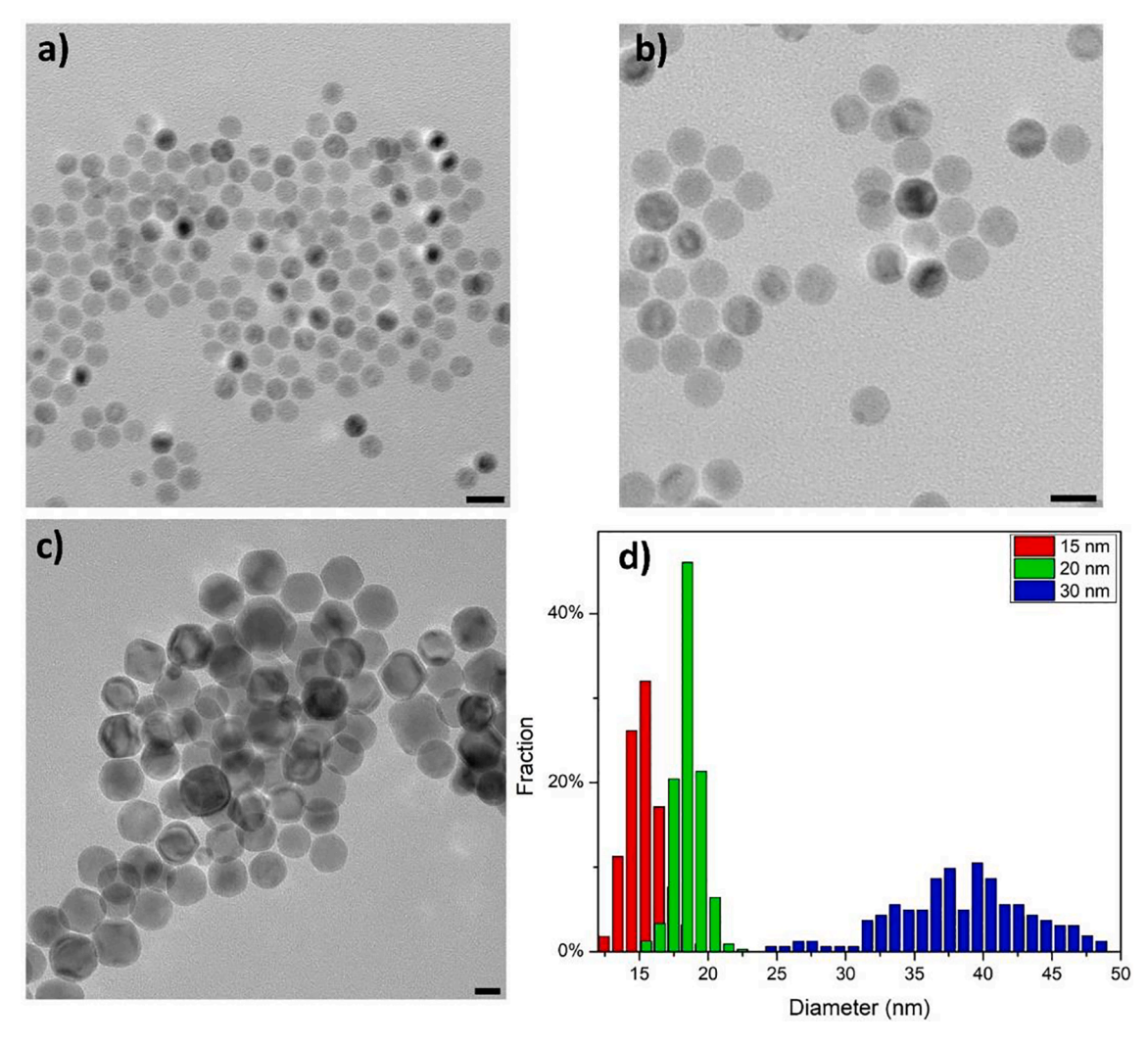


Fig. 2. TEM images of as-prepared iron oxide nanoparticles. a)  $15.4 \pm 1.3$  nm (targeted 15 nm); b)  $18.6 \pm 1.2$  nm (targeted 20 nm); and c)  $38 \pm 7$  nm (targeted 30 nm). Scale bars are 20 nm.

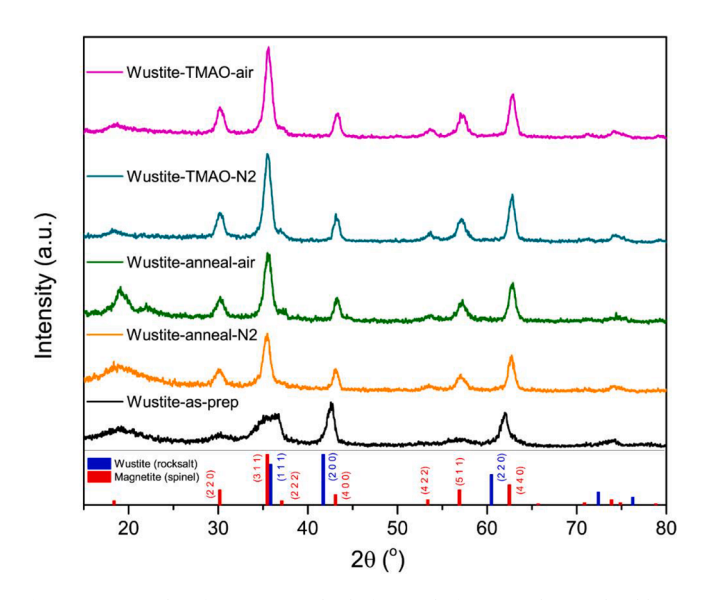


Fig. 3. XRD results of 15 nm particles before and after annealing with addition of oxidizing agents.

with larger sizes were made. Larger particles have better XRD signal-tonoise ratio and sharper peaks which will make the quantitative analysis more persuasive. Moreover, the annealing process needs to be optimized before establishing it as a standard operating procedure. Therefore, the as-prepared 30 nm iron oxide nanoparticles were annealed at three different temperatures for 1 h and 1.5 h. The 30 nm particles were selected because they have the lowest specific surface area among the three batches, and intuitively the 30 nm batch should have the purest phase as prepared. Moreover, for a post-reaction oxidation process, the larger the particles are, the longer time it will take to complete the process [24]. Therefore if the procedure works for large particles it should apply for smaller ones. The products after annealing were analyzed by XRD and Rietveld refinement to know the efficiency of annealing with different parameters. The results are shown in Table 1 and the XRD results of the sample annealed at 265°C are shown in Fig. 4. The diffraction patterns of samples annealed at different temperatures

**Table 1**The weight percentage of spinel and rock salt phases in 30 nm particles before and after annealing.

|           | As-prep | 250 °C |       | 265 °C |       | 280 °C |       |
|-----------|---------|--------|-------|--------|-------|--------|-------|
|           |         | 1 h    | 1.5 h | 1 h    | 1.5 h | 1 h    | 1.5 h |
| Spinel    | 16.0%   | 75.6%  | 97.4% | 75.3%  | 97.6% | 71.8%  | 97.0% |
| Rock salt | 84.0%   | 24.4%  | 2.6%  | 24.7%  | 2.4%  | 28.2%  | 3.0%  |

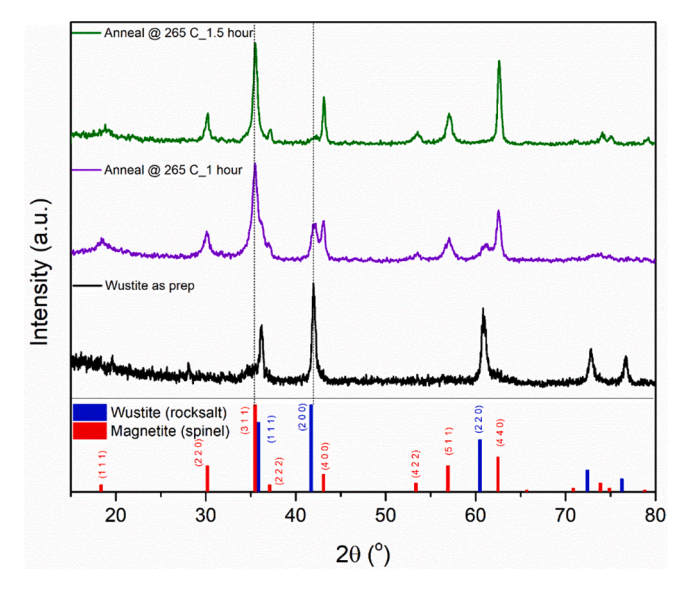
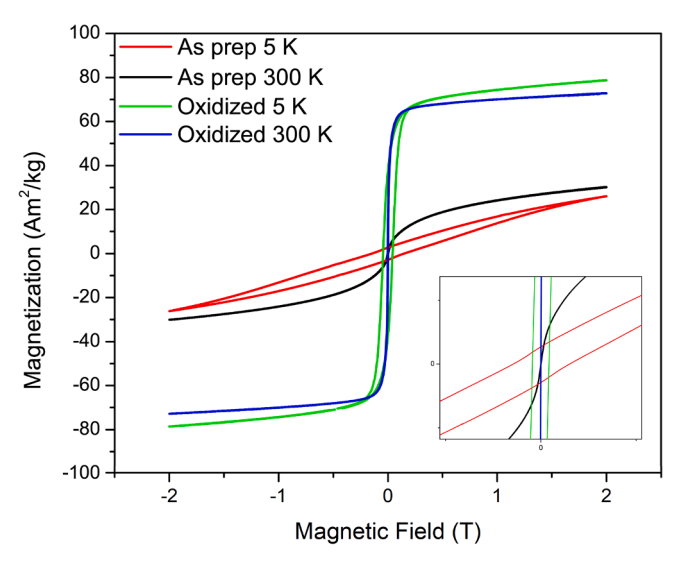


Fig. 4. XRD result of 30 nm iron oxide particles annealed at 265 °C.

are very similar if the annealing times are the same. It seems that the annealing time plays a more significant role in the phase transition, which makes sense as the kinetics of this thermo dynamically driven processes are more dominated by time if the thermal energy surpasses a minimum threshold. For example, the sharp wüstite peaks from the asprepared 30 nm sample after 1 h of annealing, the rock salt phase was partially converted to spinel phase, and if we kept annealing the sample for another half hour, the particles became nearly pure spinel. As the annealing time increases, the peaks with low-intensities started to appear in the diffractogram, such as the peaks at 18° and 75°. The 30 nm particles provided clearer XRD results which illustrated the phase transition process during annealing. It is worth emphasizing that the 30 nm samples were annealed under constant nitrogen flow without the addition of oxidizing agents. This phenomenon validates the former hypothesis, meaning the wüstite-rich particles can be successfully oxidized to spinel iron oxide particles by annealing. Considering a study on the oxidation of unsaturated aliphatic acid [25], the oleic acid could be oxidized by the oxygen in the air at high temperature and cause interparticle crosslinking, so the annealing was done under nitrogen. As discussed in the study by Kemp et al. [5] the unsaturated solvent noctadecene can be another cause for the reduction of iron. Thus, for the annealing process, n-octyl ether was selected as solvent. It was also mentioned in their study that the iron (II content increased when the temperature increased. Therefore, further annealing was done under nitrogen at 250 °C for 2 h in n-octyl ether. 20 nm as-prepared iron oxide nanoparticles were treated using this procedure, and the XRD results and the Rietveld refinement are shown in Fig. 5. The as-prepared sample consisted of both wüstite phase (68 wt%) and magnetite phase (32 wt%), while after annealing, the 20 nm sample was successfully oxidized to 100 wt% magnetite. The crystallite sizes of the as-prepared and oxidized 20 nm sample were calculated using the highest peaks and the results are shown in Table 2.

## 3.2. The effect of post-synthesis annealing on the magnetic properties

As wüstite is antiferromagnetic, the magnetic properties of the particles before and after oxidation should be very different. To show the effectiveness of oxidation and the change in magnetic properties after treatment. 20 nm iron oxide particles were measured with VSM at 5 K and 300 K under a maximum field of 2T (1495400 A/m). The magnetization curves were plotted in Fig. 5. The oxidized sample showed higher saturation magnetization and susceptibility than the as-prepared sample since magnetite contributes more magnetic moments than

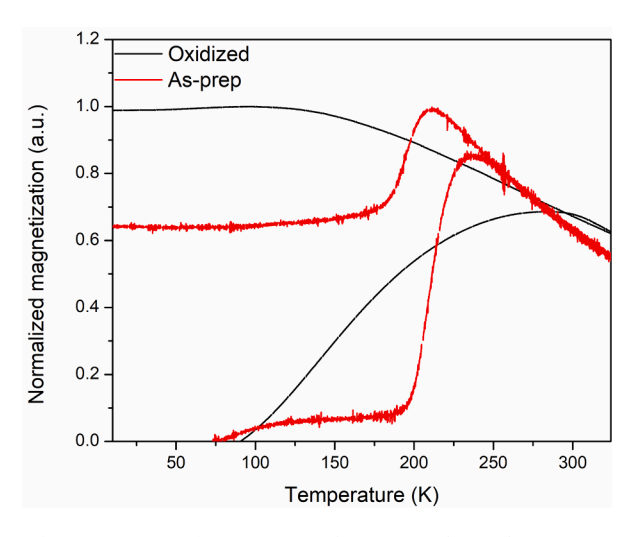


**Fig. 5.** Magnetization curves of 20 nm particles before and after oxidation. The inset shows the curves at the region close to zero field. Both as-prepared and oxidized samples showed a superparamagnetic behavior at 300 K. The saturation magnetization of as prepared sample is 30  $\text{Am}^2/\text{kg}$  (300 K), and the saturation magnetization of oxidized sample is 72  $\text{Am}^2/\text{kg}$  (300 K). The coercivity of as prepared sample is 145 mT (116000 A/m) (5 K) and coercivity of oxidized sample is 43 mT (34300 A/m) (5 K).

**Table 2**Crystallite size and composition analysis results of 20 nm sample from the XRD data

|                     | Magnetite (311)          |                      | Wüstite (200)         |                      |  |
|---------------------|--------------------------|----------------------|-----------------------|----------------------|--|
|                     | Crystallite size<br>(nm) | Percentage<br>(wt.%) | Crystallite size (nm) | Percentage<br>(wt.%) |  |
| As-prep<br>Oxidized | 3.6<br>14.8              | 32<br>100            | 11.5                  | 68                   |  |

wüstite. Both samples exhibited superparamagnetic behavior at 300 K showing no coercivity. However, at 5 K, the as-prepared sample had a coercivity around 145 mT (116000 A/m) larger than the coercivity of the oxidized sample, 43 mT (34300 A/m). This phenomenon was also seen in previous studies [26-28], which can be explained by exchange coupling between the antiferromagnetic core and the ferrimagnetic shell. The ZFC/FC measurement was conducted in a 10 mT (7977 A/m) field and the magnetization vs temperature curves are plotted in Fig. 6. As seen in Fig. 6, the curves of the two samples look very different. The FC curve of the as-prepared sample showed a drop in magnetization at around 210 K when cooling down from 325 K, while the annealed sample's magnetization kept increasing till a plateau. This phenomenon is commonly seen in the antiferromagnetic materials. When the temperature is above its Néel temperature the material behaves paramagnetically, and all the magnetic moments are magnetized to align with the field. [16,27] However, below its Néel temperature the material returns to its antiferromagnetic structure resulting in a loss of total magnetization. This result coincides with the conclusion from the structural characterizations: the as-prepared sample has a combination of wüstite and magnetite. The ZFC curves of the two samples are plotted in Fig. 6 (right). To get the Néel temperature and the blocking temperature, two regimes were used [29,30]. If the vertex of the ZFC curve was used to define the blocking temperature, the blocking temperatures are 235 K and 283 K for the as-prepared and oxidized samples, respectively. If the vertex of the derivative curve was used to define the blocking temperature, then the blocking temperatures are 209 K and 139 K, respectively, as seen in Table 3. With the same rationale, we can estimate the Néel temperature of the as-prepared sample by measuring the



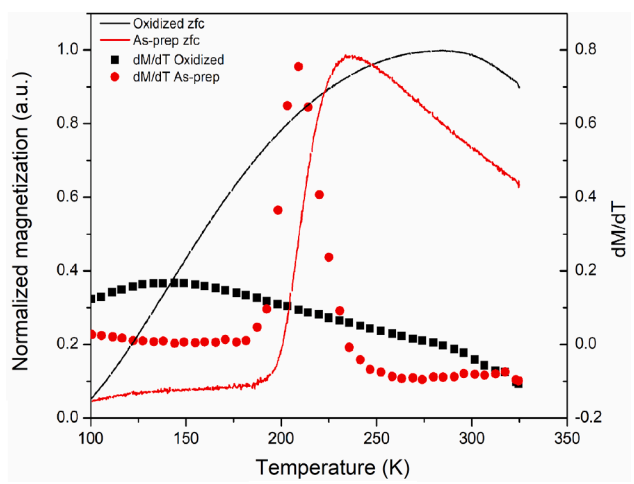


Fig. 6. Left: ZFC/FC curve of 20 nm iron oxide nanoparticles. Right: ZFC magnetization vs temperature curve and derivative of magnetization vs temperature curve.

Table 3 Summary of Néel temperature  $(T_N)$  and Blocking temperature  $(T_B)$  obtained from ZFC/FC curves.

|          | Néel temperature T <sub>N</sub> (K) |            | Blocking temperature T <sub>B</sub> (K) |            |  |
|----------|-------------------------------------|------------|---|------------|--|
|          | Max point                           | Derivative | Max point                               | Derivative |  |
| As-prep  | 210                                 | 194        | 235                                     | 209        |  |
| Oxidized | \                                   | \          | 283                                     | 139        |  |

FC curve. The results are shown in Table 3, and are comparable with the reported Néel temperature of bulk wüstite (198 K) [31]. The Néel temperature refers to the critical temperature when the thermal energy becomes high enough to disorder the anti-parallel magnetic moments that are held together by exchange interactions [32]. Therefore, only particles with an antiferromagnetic structure show a Néel temperature, and there is no Néel temperature listed in the table for the oxidized sample. The 20 nm particles were dissolved in toluene with a magnetic core concentration of 4 mg/mL and then measured under a 212 kHz, 26 kA/m (33 mT) AC field. The temperature profile is plotted in Fig. 7. The as-prepared sample did not show a temperature increase, while the oxidized sample heated from 37 °C to 63 °C within 2 min. The specific absorption rate (SAR) was calculated (linear fitting of the first 6 data

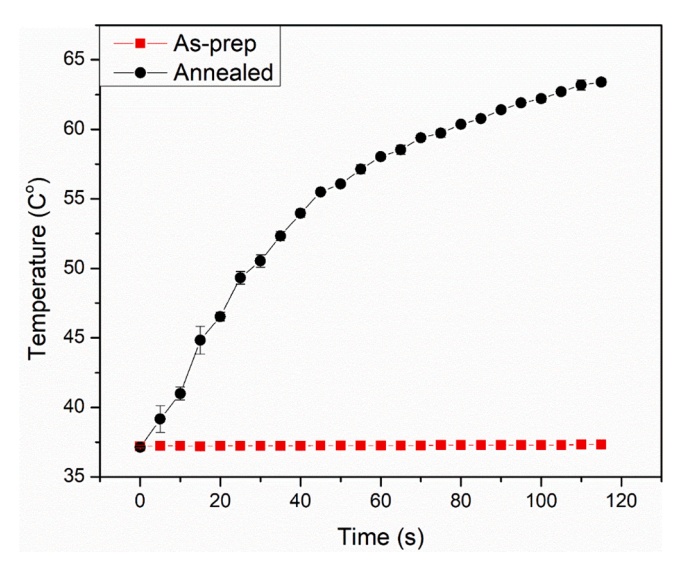


Fig. 7. Heating profile of 20 nm iron oxide particles under a 212 kHz, 33 mT AC field.

points) to be 181 W/g using [33-36]

$$SAR = \frac{\rho C \cdot \Delta T}{m \cdot \Delta t}$$

where C is the heat capacity of the measured mixture (close to the heat capacity of toluene, 1.71 J/g•K),  $\rho$  is the density of the solvent used (0.867 g/mL for toluene), m is the concentration of magnetic nanoparticles in the measured suspension (4 mg/mL), and  $\Delta T/\Delta t$  is the slope of the fitted line (0.4893 K/s in Fig. 7). The wüstite-rich particles (without post-synthesis annealing) showed no heating (SAR = 0) under such a condition (212 kHz, 26 kA/m). Previous reports showed a SAR (130 W/g) for iron oxide nanoparticles with a similar size (17  $\pm$  0.1 nm) under an AMF (205 kHz, 20 mT) [37]. A study on the commercialized iron oxide nanoparticles (25 nm) showed SAR values close to our sample (Sigma Aldrich 900026: 145.6  $\pm$  6.3 W/g and Sigma Aldrich 900027:  $176.2 \pm 27.1 \text{ W/g}$ ) under an AMF (223 kHz/, 41 kA/m) [35]. Since SAR is related to the size of the nanoparticles and the field parameters, it is better to compare SAR with the same field parameters to compare the heating efficiency of the particles. Comparing to the previous study using the same field parameters, the annealed 20 nm particles showed better heating efficiency, and the SAR is increased more than four times (20 nm, SAR = 40 W/g) [38]. Thus, post-synthesis annealing significantly improved the heating efficiency.

# 4. Conclusion and outlook

Iron oxide nanoparticles with different diameters that are rich in the wüstite phase can be oxidized by post-synthesis annealing without the addition of oxidizing agents. The XRD results showed that the oxidized particles have a pure magnetite structure. The saturation magnetization of the particles increased after annealing. The magnetic heating ability significantly increased after annealing compared to the untreated particles. With the success in the oxidation of iron oxide particles, more studies need to be done to see if the same strategy applies for substituted ferrites, such as  $\rm MnFe_2O_4$ ,  $\rm CoFe_2O_4$ , and  $\rm NiFe_2O_4$  to ensure pure spinel phase nanoparticles.

# CRediT authorship contribution statement

**Zichun Yan:** Project administration, Conceptualization, Methodology, Investigation, Data curation, Writing – original draft, Writing – review & editing. **Sara FitzGerald:** Data curation. **Thomas M. Crawford:** Supervision, Funding acquisition. **O. Thompson Mefford:** Supervision, Project administration, Funding acquisition, Writing – review & editing.

#### **Declaration of Competing Interest**

The authors declare that they have no known competing financial interests or personal relationships that could have appeared to influence the work reported in this paper.

#### Acknowledgements

ZY and OTM would like to thank the support by Materials Assembly and Design Excellence in South Carolina (MADE in SC), National Science Foundation award #OIA-1655740 Grants for Exploratory Academic Research (GEAR). The imaging was funded by Clemson Core Incentivized Access (CU-CIA). TMC and SLF acknowledge support from NSF DMR award # 1808426 and OIA award # 1655740.

#### References

- [1] W.W. Yu, J.C. Falkner, C.T. Yavuz, V.L. Colvin, Synthesis of monodisperse iron oxide nanocrystals by thermal decomposition of iron carboxylate salts, Chem. Commun. 10 (2004) 2306–2307.
- [2] J. Park, et al., Ultra-large-scale syntheses of monodisperse nanocrystals, Nat. Mater. 3 (2004) 891–895.
- [3] S. Sun, et al., Monodisperse MFe2O4 (M = Fe Co, Mn) Nanoparticles, J. Am. Chem. Soc. 126 (2004) 273–279.
- [4] E.C. Vreeland, et al., Enhanced Nanoparticle size control by extending LaMer's mechanism, Chem. Mater. 27 (2015) 6059–6066.
- [5] S.J. Kemp, R.M. Ferguson, A.P. Khandhar, K.M. Krishnan, Monodisperse magnetite nanoparticles with nearly ideal saturation magnetization, RSC Adv. 6 (2016) 77452–77464.
- [6] H.T. Hai, et al., Journal of Colloid and Interface Science Size control and characterization of wustite (core)/spinel (shell) nanocubes obtained by decomposition of iron oleate complex, J. Colloid Interface Sci. 346 (2010) 37–42.
- [7] M.J. Benitez, et al. Structural and magnetic characterization of self-assembled iron oxide nanoparticle, (2011). doi:10.1088/0953-8984/23/12/126003.
- [8] C.J. Chen, H.Y. Lai, C.C. Lin, J.S. Wang, R.K. Chiang, Preparation of monodisperse iron oxide nanoparticles via the synthesis and decomposition of iron fatty acid complexes, Nanoscale Res. Lett. 4 (2009) 1343–1350.
- [9] C.J. Chen, R.K. Chiang, H.Y. Lai, C.R. Lin, Characterization of monodisperse wüstite nanoparticles following partial oxidation, J. Phys. Chem. C 114 (2010) 4258-4263
- [10] J.-T. Jang, H. Nah, J.-H. Lee, S. Moon, M. Kim, J. Cheon, Critical enhancements of MRI contrast and hyperthermic effects by dopant-controlled magnetic nanoparticles, Angew. Chem. Int. Ed. 48 (7) (2009) 1234–1238.
- [11] C.L. Dennis, R. Ivkov, Physics of heat generation using magnetic nanoparticles for hyperthermia, Int. J. Hyperth. 29 (2013) 715–729.
- [12] C. Blanco-Andujar, A. Walter, G. Cotin, C. Bordeianu, D. Mertz, D. Felder-Flesch, S. Begin-Colin, Design of iron oxide-based nanoparticles for MRI and magnetic hyperthermia, Nanomedicine 11 (14) (2016) 1889–1910.
- [13] R. Hufschmid, H. Arami, R.M. Ferguson, M. Gonzales, E. Teeman, L.N. Brush, N. D. Browning, K.M. Krishnan, Synthesis of phase-pure and monodisperse iron oxide nanoparticles by thermal decomposition, Nanoscale 7 (25) (2015) 11142–11154.
- [14] T.H. Shin, Y. Choi, S. Kim, J. Cheon, Recent advances in magnetic nanoparticle-based multi-modal imaging, Chem. Soc. Rev. 44 (2015) 4501–4516.
- [15] M. Unni, A.M. Uhl, S. Savliwala, B.H. Savitzky, R. Dhavalikar, N. Garraud, D. P. Arnold, L.F. Kourkoutis, J.S. Andrew, C. Rinaldi, Thermal decomposition

- synthesis of iron oxide nanoparticles with diminished magnetic dead layer by controlled addition of oxygen, ACS Nano 11 (2) (2017) 2284–2303.
- [16] E. Wetterskog, C.-W. Tai, J. Grins, L. Bergström, G. Salazar-Alvarez, Anomalous magnetic properties of nanoparticles arising from defect structures: Topotaxial oxidation of Fe1- xO|Fe 3-804 core|shell nanocubes to single-phase particles, ACS Nano 7 (8) (2013) 7132–7144.
- [17] K. Davis, et al., The effect of post-synthesis aging on the ligand exchange activity of iron oxide nanoparticles, J. Colloid Interface Sci. 511 (2018) 374–382.
- [18] C. Cavelius, K. Moh, S. Mathur, Chemically designed growth of monodisperse iron oxide nanocrystals, Cryst. Growth Des. 12 (2012) 5948–5955.
- [19] Y. Meng, et al., Prediction on morphologies and phase equilibrium diagram of iron oxides nanoparticles, Appl. Surf. Sci. 480 (2019) 478–486.
- [20] G. Ketteler, W. Weiss, W. Ranke, R. Schlögl, Bulk and surface phases of iron oxides in an oxygen and water atmosphere at low pressure, Phys. Chem. Chem. Phys. 3 (2001) 1114–1122.
- [21] Aidin Lak, Mathias Kraken, Frank Ludwig, Andreas Kornowski, Dietmar Eberbeck, Sibylle Sievers, F.J. Litterst, H.W. and M.S. Size dependent structural and magnetic properties of. 12286–12295 (2013). doi:10.1039/c3nr04562e.
- [22] C.B. Kretschmer, J. Nowakowska, R. Wiebe, Solubility of oxygen and nitrogen in organic solvents from —25° to 50° C, Ind. Eng. Chem. 38 (1946) 506–509.
- [23] T. Sato, Y. Hamada, M. Sumikawa, S. Araki, H. Yamamoto, Solubility of oxygen in organic solvents and calculation of the Hansen solubility parameters of oxygen, Ind. Eng. Chem. Res. 53 (2014) 19331–19337.
- [24] L. Signorini, et al., Size-dependent oxidation in iron O

  iron oxide core-shell nanoparticles, 1–8 (2003). doi:10.1103/PhysRevB.68.195423.
- [25] N. Kalogeropoulos, F.N. Salta, A. Chiou, N.K. Andrikopoulos, Formation and distribution of oxidized fatty acids during deep-and pan-frying of potatoes, Eur. J. Lipid Sci. Technol. 109 (2007) 1111–1123.
- [26] M. Sanna Angotzi, A. Musinu, V. Mameli, A. Ardu, C. Cara, D. Niznansky, H.L. Xin, C. Cannas, Spinel Ferrite core-shell nanostructures by a versatile solvothermal seed-mediated growth approach and study of their nanointerfaces, ACS Nano 11 (8) (2017) 7889–7900.
- [27] E. Lottini, et al., Strongly exchange coupled core|shell nanoparticles with high magnetic anisotropy: a strategy toward rare-earth-free permanent magnets, Chem. Mater. 28 (2016) 4214–4222.
- [28] B.P. Pichon, et al., Microstructural and magnetic investigations of Wüstite-spinel core-shell cubic-shaped nanoparticles, Chem. Mater. 23 (2011) 2886–2900.
- [29] K.L. Livesey, et al., Beyond the blocking model to fit nanoparticle ZFC/FC magnetisation curves, Sci. Rep. 8 (2018) 1–9.
- [30] I.J. Bruvera, et al., Determination of the blocking temperature of magnetic nanoparticles: the good, the bad, and the ugly, J. Appl. Phys. 118 (2015) 1–8.
- [31] C. Kittel, Introduction to solid state physics, Sixth Ed., John Wiley & Sons. Inc., York. 2005. 1986.
- [32] N.A. Spaldin, N.D. Mathur, Magnetic materials: fundamentals and device applications, Phys. Today 56 (2003) 62–63.
- [33] I. Andreu, E. Natividad, I. Andreu, E. Natividad, Accuracy of available methods for quantifying the heat power generation of nanoparticles for magnetic hyperthermia generation of nanoparticles for magnetic hyperthermia, 6736 (2013).
- [34] L. Del Bianco, et al., Mechanism of magnetic heating in Mn-doped magnetite nanoparticles and role of the intertwined structural and magnetic properties, Nanoscale (2019) 10896–10910, https://doi.org/10.1039/c9nr03131f.
- [35] O.L. Lanier, et al., Evaluation of magnetic nanoparticles for magnetic fluid hyperthermia, Int. J. Hyperth. 36 (2019) 687–701.
- [36] D. Chang, et al., Biologically targeted magnetic hyperthermia: Potential and limitations. Front. Pharmacol. 9 (2018).
- [37] F. Reyes-Ortega, Á.V. Delgado, E.K. Schneider, B.L.C. Fernández, G.R. Iglesias, Magnetic nanoparticles coated with a thermosensitive polymer with hyperthermia properties, Polymers (Basel). 10 (2017).
- [38] S.L. Saville, et al., The formation of linear aggregates in magnetic hyperthermia: implications on specific absorption rate and magnetic anisotropy, J. Colloid Interface Sci. 424 (2014) 141–151.